Title
Ion Transport and Crystal Rotation in Plastic Crystal Electrolytes Under Applied Electric Fields

Journal
CHEMISTRY OF MATERIALS, 38(13)

ISSN
0897-4756

Authors
Yap, Kyra MK
Abdo, Emily E
Aramaki, Hiroki
et al.

Publication Date
2026-07-14

DOI
10.1021/acs.chemmater.6c00803

Ion Transport and Crystal Rotation in Plastic Crystal Electrolytes under Applied Electric Fields

Kyra M. K. Yap[1,2,‡], Emily E. Abdo[1,2,‡], Hiroki Aramaki[3], Hiroki Sugisawa[3,4], Tomofumi Hamamura[3,4], Kazunori Mukunoki[3,4], Julia Im[1], Hasan Celik[5], Sarah A. Hesse[6], Partha P. Paul[6], Nitash P. Balsara[1,2,*]

[1]Department of Chemical and Biomolecular Engineering, University of California, Berkeley, California 94720, United States

[2]Materials Sciences Division, Lawrence Berkeley National Laboratory, Berkeley, California 94720, United States

[3]Mitsubishi Chemical Center for Advanced Materials, University of California, Santa Barbara, California, 93106, United States

[4]Innovation Strategy Division, Mitsubishi Chemical Corporation, 1000, Kamoshida-cho, Aoba ward, Yokohama city, 227-8502, Japan

[5]Pines Magnetic Resonance Center, Core NMR Facility, College of Chemistry, University of California, Berkeley, California 94720, United States

[6]Stanford Synchrotron Radiation Lightsource, SLAC National Accelerator Laboratory, Menlo Park, California 94025, United States

[‡]Authors contributed equally

[*]Corresponding author email: nbalsara@berkeley.edu

Abstract

Organic ionic plastic crystal electrolytes, containing a plastic crystal and lithium salt, offer a potential balance between mechanical and electrochemical properties for solid state lithium-ion battery electrolytes. These electrolytes contain multiple mobile ionic species (three or four), resulting in complex transport mechanisms which have not yet been established. Plastic crystals are defined by long-range positional order and short-range rotational disorder. It is therefore necessary to quantify changes in the local crystal structure of the electrolyte as current flows through it. Herein, we examine the electrochemical properties of pyrrolidinium-based plastic crystal electrolytes containing lithium salt and zwitterion additives, including measurements of current fraction and limiting current. We obtain species-specific insight into electrolyte transport using pulsed-field gradient nuclear magnetic resonance spectroscopy and find that, while the zwitterion additive increases ionic conductivity, it decreases lithium diffusivity with respect to other ionic components. With *operando* spatiotemporally resolved wide angle X-ray scattering we observe location-specific crystal rotations due to the passage of ionic current. We posit that reducing energy dissipation due to rotation is essential for using plastic crystal electrolytes in practical applications.

Introduction

Traditional liquid electrolytes for rechargeable lithium-ion batteries are mixtures of organic solvents and salts.[1] There is considerable interest in developing new electrolytes for rechargeable batteries as they could enable an increase in energy density and improvement in safety.[2,3] Inorganic crystalline electrolytes are one attractive alternative offering comparable ionic conductivity to traditional liquid electrolytes.[4–6] These crystalline electrolytes are characterized by high storage modulus which enables coupling with high-capacity electrodes such as lithium metal anodes.[7,8] However, limitations to their application arise due to their non-compliant nature, driven by losses of contact between the electrode and electrolyte as battery electrodes expand and contract during operation.[9,10] Organic ionic plastic crystal electrolytes, comprising mixtures of a plastic crystal and salt, appear to be a natural bridge between liquid electrolytes and inorganic crystalline electrolytes. The compliance of these electrolytes may enable better electrode/electrolyte contact and their solid-like mechanical properties may enable coupling with high-capacity and high energy density electrodes.[11–14] Yet, a major limitation to the application of plastic crystal electrolytes is their conductivity, which is significantly lower than that of both liquid and crystalline electrolytes.[5,13,15,16] The reason for poor ion transport in plastic crystal electrolytes has not yet been established.

Salts comprising a bulky organic cation and inorganic anion naturally self-assemble to form solid plastic crystals. Examples of cations include ammonium,[17,18] phosphonium,[19–22] and pyrrolidinium[23,24], coupled to anions including bis(fluorosulfonyl)imide (FSI^-), bis(trifluoromethanesulfonyl)imide ($TFSI^-$), and tetrafluoroborate (BF_4^-). These crystals exhibit an intermediate plastic crystal phase, which exists between the liquid and crystalline phases, and is defined by long-range order and short-range rotational disorder.[11,14] When mixed with a lithium salt, the mixture comprises only charged species (three or four), making them fundamentally different from traditional liquid electrolytes based on neutral organic solvents. In principle, all species in a plastic crystal electrolyte are mobile and can translate under an applied electric field. In contrast, only the cation is translationally mobile in inorganic crystalline electrolytes.

The passage of current through inorganic crystalline electrolytes occurs without the formation of concentration gradients due to electroneutrality.[25] Since the anions cannot translate, the concentration of cations must be uniform even as current passes through the electrolyte. In contrast, the passage of current through traditional liquid electrolytes containing a neutral solvent results in the formation of salt concentration gradients due to the mobility of all three electrolytic species.[26] The underpinnings of these concentration gradients have been described by Newman's concentrated solution theory.[27] Their magnitudes are governed by three transport properties, ionic conductivity, diffusion coefficient, and cation transference number, and two thermodynamic properties, the salt activity coefficient and the partial molar volume of the salt. Interest in quantifying concentration gradients arises from the fact that the motion of all species other than the working lithium ion results in energy dissipation and a reduction of battery efficiency.[28] While

concentration gradients could exist in plastic crystal electrolytes, due to the mobile nature of all species, there is no systematic understanding of the phenomena which drive their development. Moreover, the presence of long-range order requires the development of models that go beyond Newman's concentrated solution theory. For example, when current is passed through the electrolyte, fundamentally different plastic crystal phases may form locally within the electrolyte due to the presence of salt concentration gradients.

In a symmetric Li/electrolyte/Li cell containing a traditional liquid electrolyte, the magnitude of concentration gradients increases with increasing applied current. The current density at which the salt concentration at the negative electrode at steady-state approaches zero is called the limiting current. If the applied current exceeds the limiting current, then the cell voltage diverges at a time called the Sand's time.[29] The Sand's time is a measure of the time required for the salt concentration at the negative electrode to approach zero. To our knowledge, neither limiting current nor Sand's time has been measured in any plastic crystal electrolyte.

In this study, we explore the ion transport properties for ternary organic ionic plastic crystal electrolytes, containing *N,N*-diethylpyrrolidinium bis(fluorosulfonyl)imide ([C_2epyr][FSI]), lithium bis(fluorosulfonyl)imide (LiFSI), and a zwitterionic (ZI) additive. Previous studies suggest that zwitterion additives lead to enhanced ion dissociation, improved battery cycling, and increased electrolyte stability against lithium metal.[30–33] We examined electrolytes with varying molar ratios of [LiFSI]/[ZI] – 5/10, 5/20, 10/10, and 15/20 – to explore how the addition of salt and zwitterion additives impacted the thermal, morphological, and electrochemical properties of these electrolytes. We employed pulsed-field gradient nuclear magnetic resonance spectroscopy (PFG-NMR) to provide species-specific insight into ion transport. Finally, we conducted *operando* wide angle X-ray scattering (WAXS) to probe morphological changes to the electrolyte under the passage of ionic current. Our findings indicate that ionic conductivity increases with increasing zwitterion concentration, but that Li^+ transference, and in turn practical battery performance, is heavily compromised. We measure the Sand's time and limiting current using lithium symmetric cells to quantify battery performance. PFG-NMR confirms the sluggish diffusivities of Li^+. *Operando* WAXS measurements unveil the presence of current-induced crystal grain rotations which could serve as an additional pathway for energy dissipation.

Methods

Electrolyte Preparation

Electrolytes containing [C_2epyr][FSI] with 5/10, 5/20, 10/10, 15/20 ratios of [LiFSI]/[ZI] were prepared by Mitsubishi Chemical Corporation. The electrolytes are named such that the first number refers to the moles of LiFSI and the second number refers to the moles of zwitterion on a 100-mole basis of [C_2epyr][FSI]. For example, the 5/10 electrolyte comprises a mole ratio of 5 moles LiFSI, 10 moles zwitterion, and 100 moles [C_2epyr][FSI]. The electrolytes were made by

melting [C_2epyr][FSI] at 140°C, and then adding the zwitterion, ((3-(1-methylpyrrolidin-1-ium-1-yl)propyl)sulfonyl)((trifluoromethyl)sulfonyl)imide (for simplicity, we refer to this compound as ZI). The mixture was left at 140°C for an hour. Following this, LiFSI was added and the mixture was stirred at 140°C for an additional hour. The electrolyte was then allowed to cool to room temperature. Upon receipt at UC Berkeley, the electrolytes were dried at 60°C overnight under vacuum prior to use. All sample preparations for DSC, WAXS, NMR, or electrochemical measurements were conducted within an argon glovebox with O_2 < 1 ppm and H_2O < 1 ppm.

Density measurements

The room temperature density (ρ) of [C_2epyr][FSI] at each [LiFSI]/[ZI] composition was measured by weighing a 40 µL pan filled with electrolyte. This was repeated in triplicate for each sample, and results are summarized in Table S1. The lithium salt concentration of each electrolyte, c_{Li}, was calculated following:

$$c_{Li} = \frac{r_{LiFSI}\,\rho}{\left(r_{LiFSI}\,M_{LiFSI} + r_{ZI}\,M_{ZI} + M_{IPC}\right)}, \qquad \textbf{(eq. 1)}$$

where r_{LiFSI} and r_{ZI} denote the molar ratio of Li salt or zwitterion to the [C_2epyr][FSI] plastic crystal, respectively, and M_i represents the molar mass of species i in kg mol^{-1}.

Differential scanning calorimetry

DSC samples were prepared inside an argon glovebox by sealing 5 to 20 mg of electrolyte within hermetic aluminum pans (TA Instruments). Measurements were conducted at the Molecular Foundry with a TA Instruments DSC Q200 under N_2 flow. After an initial heating cycle to 150°C to erase the thermal history, the plastic crystal samples were cooled to -90°C and then heated back to 150°C at 5°C min^{-1}. This second heating cycle was reported. In the case of the 5/20 electrolyte, the second heating cycle was done at 10°C min^{-1} to obtain sharper features in the DSC trace. By convention, the first phase below the liquid phase (L) is denoted as plastic crystal phase I.

Wide-angle X-ray scattering

Ex situ and *operando* WAXS measurements were conducted at the Stanford Synchrotron Radiation Lightsource (SSRL) beamline 11-3. The X-ray energy was fixed at 12.7 keV, and diffractograms were collected on a Rayonix MX225 CCD area detector. The sample-to-detector distances and detector tilts were calibrated for the *ex situ* and *operando* experiments using a lanthanum hexaboride standard, and *ex situ* scans were collected with a 1 s exposure time. Data were collected at room temperature (25°C). *Ex situ* cells were assembled inside a glovebox by placing electrolyte in airtight aluminum holders with polyimide windows. The 2D intensities recorded on the area detector were integrated using the Nika program for IGOR Pro to yield intensity I as a function of scattering vector, q, and azimuthal angle, χ.[34]

Operando Swagelok style cells comprising lithium indium symmetric cells were housed in a custom polycarbonate holder. 40 mol% lithium indium (LiIn) alloy electrodes were fabricated according to the procedure outlined in ref. 35.[35] To assemble the *operando* cells, electrolyte was placed within a polycarbonate spacer (McMaster-Carr) and sandwiched between two LiIn electrodes. The ensemble was placed within the custom polycarbonate holder and screwed into place with stainless steel core pins (McMaster-Carr) and PEEK nuts (IDEX). The cells resemble those depicted in ref. 34[35] – the main difference between the setups was the use of amorphous polycarbonate for the holder and washer material to reduce the appearance of sharp WAXS peaks from the cell body. Moreover, the polycarbonate washer was thinned down to a thickness of 0.5 mm around the electrolyte to minimize the X-ray path length through the cell body.

The *operando* WAXS experiment was performed by mounting the cell onto a vertical stage and connecting it to a portable Biological VSP300 potentiostat placed inside the hutch. During the experiment, the cell was moved in 50 μm increments along the electrolyte from one electrode to the other (*x*-direction). X-rays passed through the electrolyte, parallel to the electrodes, and the beam profile was 50 μm tall and 300 μm wide. Scattering measurements were collected at seven locations along the electrolyte. At each cell position, images were acquired with a 30 s exposure time every 20 min.

Data analysis was performed using the pyFAI library in python.[36] Scattering images were integrated to yield 2-dimensional (χ, q) plots using the pixel-splitting method with 360 azimuthal sectors in χ and 1,024 rings in q. To obtain azimuthally-averaged $I(q)$ spectra, intensities from the 2-dimensional (χ, q) data were filtered to remove any bright streaks and then summed over the entire χ range at each value of q. To obtain $I(\chi)$ spectra, the raw intensities from the 2-dimensional (χ, q) data were summed over a specific value of q (e.g. 0.85 $Å^{-1}$) ± 0.01 $Å^{-1}$. Changes in the location of peaks in $I(q)$ generally signal phase changes (e.g. appearance or disappearance of plastic crystal phase), while changes in $I(\chi)$ generally signal crystal rotations. The intensities reported are not transmission-corrected. Due to the lithium indium electrodes and the stainless-steel plungers, regions of χ were obscured depending on the measurement position. An example of the data analysis workflow for data acquired at t = 0.3 h and at x/L = 0.8 is provided in **Figure S14**.

Electrochemical measurements

Conductivity

Conductivity measurements were conducted in coin cells assembled using CR2032 coin cell components (Hohsen Corp). Electrolyte was added to an adhesive silicone spacer with a thickness of 500 μm and an inner diameter of 3.175 mm (McMaster-Carr) and sandwiched between 500 μm blocking stainless-steel electrodes (MTI). A stainless-steel wave spring (MTI) was placed on top of the stack, and the coin cells were sealed with a crimper (MTI). Conductivity, κ, was measured in a Jeio Tech TC-ME-100 environmental chamber at three temperatures (30, 50, 70, 90°C). The

temperature was verified with the use of a thermocouple. The cells were allowed to equilibrate for 30 min at temperature before the experiments were conducted. AC impedance spectroscopy was conducted using a Biologic VMP300 potentiostat, using a frequency range of 1 MHz to 100 mHz and a sinus amplitude of 80 mV. The bulk resistance, R_b, was obtained from the Nyquist plot of the impedance spectra. Conductivity was calculated from the measured R_b according to:

$$\kappa = \frac{L}{R_b A}\ , \qquad \textbf{(eq. 2)}$$

where L is the thickness of the separator (cm) and A is the surface area of the electrodes (cm^2).

Current fraction

To prepare Li symmetric cells , Li chips (MTI) were brushed on both sides and then pressed with a hand press until shiny. Electrodes with a diameter of 6 mm were punched out and affixed onto stainless steel shims (MTI) by pressing between pouch material with a hand press. Electrolyte was placed in the adhesive silicone spacers and sandwiched between Li electrodes to form the coin cell stack and crimped. Assembled cells were preconditioned by applying a current of +/- 0.1 uA cm^{-2} for 12 h, for a minimum of 4 cycles until a stable interfacial resistance, R_i, was reached. Current fraction measurements were carried out using the Bruce-Vincent method,[37] wherein a voltage of +10 mV was applied for 13.7 h, with impedance measurements collected every 20 min, and then the cell was allowed to relax for 12 h at open-circuit voltage. This process was repeated at -10 mV. The current fraction was calculated according to **eq. 3**:

$$\rho_{+¿} = \frac{i_{ss}(\Delta V - i_\Omega R_{i,0})}{i_\Omega(\Delta V - i_{SS} R_{i,SS})}¿\ , \qquad \textbf{(eq. 3)}$$

where i_Ω is calculated by **eq. 4**:

$$i_\Omega = \frac{\Delta V}{R_{b,0} + R_{i,0}}\ . \qquad \textbf{(eq. 4)}$$

Where ΔV is the applied voltage (V), the subscripts b and i refer to the bulk and interfacial resistances respectively, and the subscripts 0 and SS refer to initial and steady-state measurements respectively.

Restricted diffusion

The diffusion coefficient was calculated using the restricted diffusion approach.[38] The open-circuit relaxation potential following the current fraction experiment was fit to an exponential form (**eq. 5**):

$$U(t) = k_0 + a e^{-bt}, \quad \textbf{(eq. 5)}$$

where the diffusion coefficient, D, is related to the coefficient, b, by:

$$D = \frac{L^2 b}{\pi^2}. \quad \textbf{(eq. 6)}$$

Where L is the thickness of the electrolyte (cm).

Limiting current via Sand's time

The thickness-normalized limiting current of each electrolyte was measured at 30°C using the Sand's time approach described previously.[29] Following measurement of current fraction, multiple current densities were applied to the Li-Li symmetric cells for 12 h followed by an 18 h relaxation period back to open-circuit potential and an impedance measurement to ensure no significant changes to bulk or interfacial resistance. The current density was increased until potential divergence occurred for a minimum of four different current densities. The limit of potential divergence was set to 1 V and the time taken for the potential to diverge was recorded as the Sand's time. To estimate the limiting current density, we adopted the linear approach reported by Hoffman et al.[29]

All electrochemical data were collected and analyzed with the EC Lab software.

Pulsed field gradient NMR

NMR samples were prepared by loading electrolyte into 5 mm NMR tubes. The electrolytes were melted at 150°C before being sealed under an argon atmosphere to reduce void space formation. Self-diffusion coefficients were measured using pulsed field gradient NMR at a field strength of 9.4 T on a Bruker Avance IV NEO (400.23 MHz for ^{1}H, 155.54 MHz for ^{7}Li, and 376.59 MHz for ^{19}F) spectrometer fitted with a 5 mm double resonance broad band diffusion probe (diffBB) equipped with a z-axis gradient. The diffBB probe had a maximum gradient strength of 17 T/m and a Great60 amplifier was used to generate the gradient pulses. Sample temperature was calibrated using an ethylene glycol sample (80%) in DMSO-d_6 (20%). Diffusion coefficients were measured at 30, 50, 70, and 90°C, with an equilibration period of 20 min. A standard diffusion double stimulated echo sequence (diffDsteAV3) using sine shaped magnetic field gradient pulses was employed with application of 16 dummy scans at the beginning of spectral acquisition and 8 scans (^{1}H, ^{19}F) or 256 scans (^{7}Li) per gradient amplitude. 16 gradient strengths (g), in equally spaced increments, were applied to achieve optimal signal attenuation. The range of maximum gradient strengths was varied up to 1400 G cm^{-1} for different nuclei and different temperatures to optimize signal attenuation. For ^{1}H and ^{19}F experiments, a 1-1.5 ms gradient pulse application duration (δ), 100-200 ms diffusion

time (Δ), 5 s repetition time, 100 μs gradient pulse stabilization delay (d16), and a 90° pulse duration (p1) of 15 μs at 16 W pulse power (plw1) were used. For ^{7}Li experiments, a 1-2 ms gradient pulse application duration (δ), 200-500 ms diffusion time (Δ), 10 s repetition time, 100 μs gradient pulse stabilization delay (d16), and a 90° pulse duration (p1) of 19 μs at 22 W pulse power (plw1) were used. Pulse times were varied based on the diffusion coefficient resolution required at different temperatures. Data was processed with Bruker's Topspin Software, using Dynamics Center. Peak intensities were calculated by analyzing the highest gradient slice and calculating the integral of the peak with an integral width equal to the full width of the peak at half maximum intensity. The attenuation curves of the integrated peak intensities were fit to the Stejskal–Tanner equation (**eq. 7**) for double stimulated echo sequence using sine-shaped gradient pulses.[39–41]

$$S(g)=S(0)\exp\left[-D\gamma^{2}\delta^{2}g^{2}\left(\Delta-\frac{\delta}{2}\right)\frac{4}{\pi^{2}}\right] \qquad \textbf{(eq. 7)}$$

Where $S(g)$ and $S(0)$ are the intensity of the PFG-echo profile at the gradient strengths of g and 0, respectively, D = self-diffusion coefficient (m^2 s^{-1}), γ = gyromagnetic ratio (s^{-1} G^{-1}).

Results & Discussion

We measured the thermal and structural properties of [C_2epyr][FSI] electrolytes as a function of salt and zwitterion concentration. The components of the plastic crystal electrolytes are given in **Figure 1a**, and the compositions studied in this work are given in **Table 1**. The density of the electrolytes is reported in **Table S1**. The electrolytes are named according to the molar ratio of [LiFSI]/[ZI] additive, e.g. 5/10 contains 5 moles of LiFSI and 10 moles of zwitterion on a 100-mole basis of [C_2epyr][FSI]. The thermal properties of the electrolytes, characterized by differential scanning calorimetry (DSC), are shown in **Figure 1b**. The data obtained from the 5/10, 10/10, and 15/20 electrolytes are similar. We observed a crystalline phase at low temperatures, and a sharp peak in the DSC curve signifying a phase transition to a plastic crystal phase. The solid-solid transition temperatures range from -32 to -37°C for the 5/10, 10/10, and 15/20 electrolytes. In 15/20, a subtle feature appears at -18°C. The origin of this feature remains to be established. The 5/10, 10/10, and 15/20 electrolytes exhibited melting points at 109, 87, and 72°C, respectively, indicating that increasing the concentration of the lithium salt and the zwitterion resulted in decreases in melting temperature, but did not significantly affect the crystal-to-plastic-crystal phase transition temperature. The DSC curve of the 5/20 electrolyte exhibits a broad and poorly defined crystal-to-plastic-crystal peak in the vicinity of -30°C. The temperature of this phase transition is similar to those of the other electrolytes. Additional features are seen at temperatures above 40°C in the DSC curve of the 5/20 electrolyte. The main conclusion of our DSC study is that all electrolytes exhibit a plastic crystal phase at 25°C. Following the literature,[11] we refer to this as phase I.

The DSC results shown in **Figure 1b** (except 5/20) are consistent with literature reports. In reference [24], it was shown that a [C_2epyr][FSI] electrolyte containing 5 mol% LiFSI had a melting temperature of 119°C and exhibited a plastic crystal phase at lower temperatures, including room temperature. This electrolyte composition is analogous to a 5/0 concentration and will be referred to as the 5/0 composition herein. Additionally, it was shown that increasing the concentration of LiFSI salt results in a decrease in the melting point of plastic crystal electrolytes, with a negligible change in the crystal-to-plastic-crystal phase transition temperature.[23]

The crystal structure of the electrolytes at 25°C were characterized by wide-angle X-ray scattering (WAXS) and are shown in **Figure 1c**. Characteristic peaks were observed in the 5/10, 10/10, and 15/20 electrolytes at q values of 0.87 and 1.23 Å^{-1}. These values correspond to interplanar spacings (d) of 7.22 and 5.11 Å, according to $d = 2\pi/q$. As was observed in the DSC data, the WAXS data from the 5/20 electrolyte was different from that of the other electrolytes. Scattering peaks at q values of 0.87 and 1.23 Å^{-1} were accompanied by several additional peaks, suggesting the presence of secondary phases or polymorphs.[42] The WAXS results shown in **Figure 1c** are generally similar to those reported in the literature for neat [C_2epyr][FSI] or salt-containing [C_2epyr][FSI]. In references [23,24,43] and [40], it was shown that neat [C_2epyr][FSI] exhibits two characteristic peaks in X-ray diffraction for the phase I plastic crystal. In these reports, the characteristic spacings were 7.2

and 5.1 Å for the neat material, and the presence of few peaks was attributed to a higher degree of symmetry in the phase I plastic crystal. Additionally, X-ray diffraction studies of a similar electrolyte, [C_2mpyr][FSI], in the neat state and with 10 mol% LiFSI also displayed a signature of two peaks for the phase I plastic crystal, and the interplanar spacing increased slightly with the addition of LiFSI salt.[23] Interpreting WAXS data from plastic crystals in terms of a lattice structure is nontrivial. In ref. [44], a definitive interpretation of WAXS data was only possible after a single crystal was obtained using exacting means, and X-ray diffraction measurements were collected at 100 K. There are no well-defined strategies for obtaining single crystals in these systems. We did not attempt to obtain single crystals of the electrolytes studied in this paper. To the best of our knowledge, the data in **Figure 2c** are the first WAXS measurements of zwitterion-containing [C_2epyr][FSI] electrolytes.

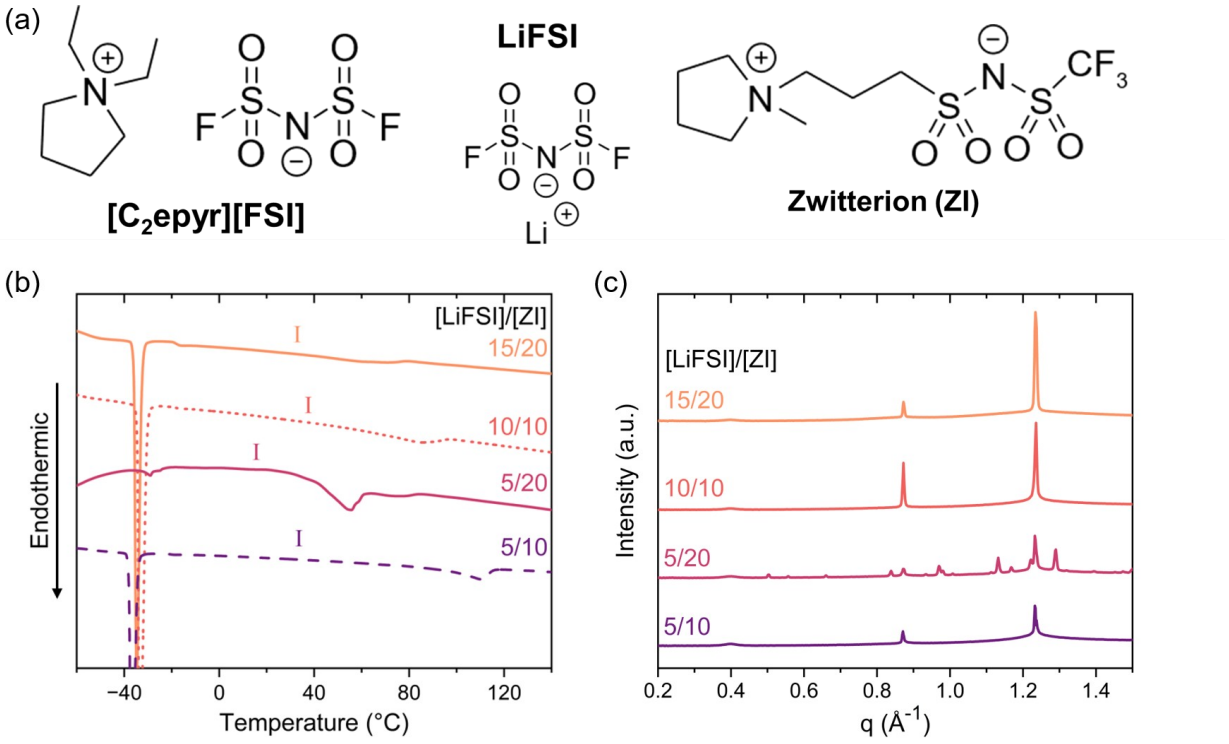

Figure 1. (a) Chemical structures of species in the plastic crystal electrolyte studied in this work. (b) Differential scanning calorimetry traces of the plastic crystal electrolytes. By convention, Phase I is designated as the first phase below the melting point. (c) *Ex situ* wide angle X-ray scattering of the plastic crystal electrolytes at 25°C.

Table 1. Composition of the [C_2epyr][FSI]/LiFSI/ZI plastic crystal electrolytes.

Electrolyte Name	[C_2epyr][FSI] (mol)	LiFSI (mol)	ZI (mol)	c_{Li+} (mol L^{-1})
5/10	100	5	10	0.18
5/20	100	5	20	0.19
10/10	100	10	10	0.38
15/20	100	15	20	0.64

Figure 2 describes the results of electrochemical characterization of the plastic crystal electrolytes. Ionic conductivity, κ, (**Figure 2a**) was measured at 30, 50, 70, and 90°C. At 30°C, the ionic conductivities for the electrolytes were 7.90×10^{-5} S cm^{-1}, 1.12×10^{-4} S cm^{-1}, 2.49×10^{-4} S cm^{-1}, and 5.19×10^{-4} S cm^{-1} for the 5/10, 5/20, 10/10, and 15/20 electrolytes, respectively. In a previous study, the ionic conductivity of [C_2epyr][FSI] mixed with 5 mol% LiFSI (5/0) at 25°C was 6.4×10^{-5} S cm^{-1} and is provided on **Figure 2a** as a reference.[24] The addition of zwitterion in the 5/10 electrolyte resulted in ionic conductivity of similar magnitude to the previously reported 5/0 electrolyte. Increasing the zwitterion concentration in the 5/20 electrolyte resulted in a modest increase in ionic conductivity. There are several reports of increased conductivities in electrolytes upon the addition of zwitterions.[30,45,46] In the materials of interest, we posit that transport is facilitated by the presence of defects induced in the [C_2epyr][FSI] crystal lattice by the zwitterions.[43,47,48] Larger increases in ionic conductivity were obtained by increasing the lithium salt concentration: the conductivity of the 15/20 electrolyte is a factor of 5 larger than that of the 5/20 electrolyte. This is consistent with previously reported observations on pyrrolidinium-based plastic crystal electrolytes mixed with alkali salts.[42,49] The relative changes in conductivity are similar in the temperature range between 30 and 70°C for all electrolytes; the electrolytes are plastic crystals in this temperature range. However, at 90°C, the conductivities of the 10/10 and 15/20 electrolytes are within experimental error. The DSC results indicate that these electrolytes are in the liquid state at this temperature.

Figure 2b shows the current fraction, $\rho_{+¿¿}$, for the plastic crystal electrolytes, as measured by the Bruce-Vincent-Watanabe method.[50–52] In conventional electrolytes comprising mixtures of a lithium salt and a solvent, current fractions deviating from unity signal the formation of salt concentration gradients that result in concentration overpotentials.[50,53] For all electrolytes in this study, $\rho_{+¿¿}$ ranges from 0.01 to 0.04. These values are an order of magnitude lower than those typically reported for plastic crystal electrolytes with similar chemistries. In particular, $\rho_{+¿¿}$ of 5/0 [C_2epyr][FSI] with LiFSI at 60°C was measured to be 0.27,[24] while that of 5/0 [C_2epyr][FSI] with $Mg(FSI)_2$ at 25°C

was measured to be 0.28.[54] In comparison, previously reported lithium transference numbers for pyrrolidinium-based ionic liquids, estimated by current fraction measurements, PFG-NMR, and electrophoretic NMR , have been observed at magnitudes similar to the $\rho_{+,i}$ observed in this work.[55–57] The reason for the differences between our measurements on plastic crystal electrolytes and the existing plastic crystal electrolyte literature remains to be established.

The diffusion coefficient, D, was measured using restricted diffusion experiments at 30°C (**Figure 2c**). D gives the diffusive flux due to driving forces that arise in the presence of a concentration gradient. For all electrolytes, D was of a similar order of magnitude, varying from 1.4 x 10^{-8} cm^2 s^{-1} in the 10/10 electrolyte to 3.1 x 10^{-8} cm^2 s^{-1} for the 5/20 electrolyte.

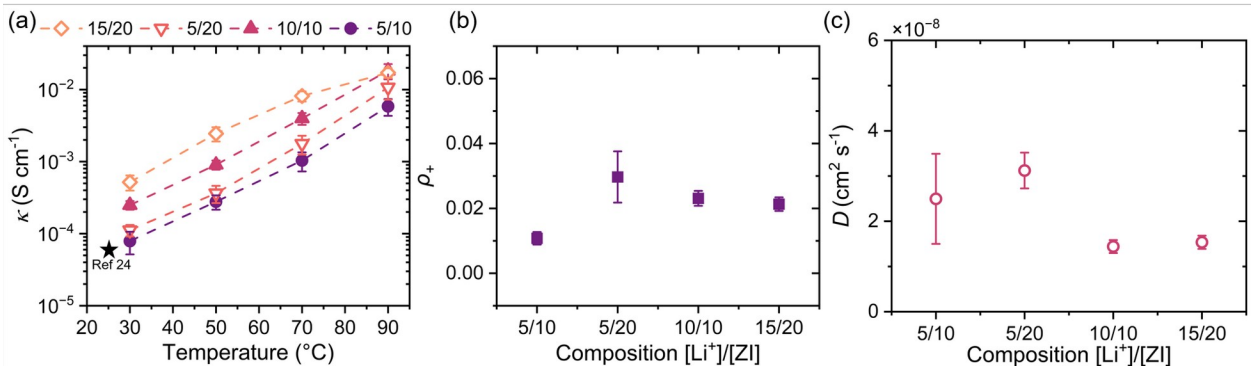

Figure 2. Experimentally measured plastic crystal electrolyte transport properties: (a) conductivity κ versus temperature, (b) current fraction $\rho_{+,i}$ versus composition, and (c) diffusion coefficient D versus composition. Experiments to determine $\rho_{+,i}$ and D were conducted at 30°C. The conductivity for a 5/0 electrolyte reported by Yamada et al.[24] at 25°C is added for reference using the star symbol. All experiments were repeated at least three times on independent cells and error bars representing one standard deviation are shown.

PFG-NMR was conducted on the ^{1}H ($D_{C_2epyr^{+},i}$), ^{7}Li ($D_{Li^{+},i}$), and ^{19}F ($D_{FSI^{-},i}$, D_{ZI}) nuclei to capture the species-specific self-diffusion coefficients for all species in the electrolytes. D_i reflects the Brownian motion of species i in the absence of concentration gradients. The self-diffusion coefficients of each species in the electrolytes are plotted as a function of temperature in **Figure 3**. Representative NMR spectra for the electrolyte species are given in **Figure S1**, and an example fit of the PFG-NMR results to the Stejskal-Tanner equation, which enables the estimation of self-diffusion coefficients, is provided in **Figure S2**. For all electrolytes, $D_{FSI^{-},i} > D_{C_2epyr^{+},i} > D_{Li^{+},i} > D_{ZI}$. In previous studies of [C_2epyr][FSI] with 10 mol% LiFSI (without zwitterion), the order of self-diffusion coefficients was $D_{FSI^{-},i} > D_{Li^{+},i} > D_{C_2epyr^{+},i}$.[43] It appears that the addition of zwitterion slows down the diffusion of Li^+ relative to the other ionic components in the electrolyte. The addition of zwitterion slows down the diffusion of all ionic species; compare the 5/10 data in **Figure 3a** and the 5/20 data in **Figure 3b**. In contrast, the addition of lithium salt hastens the diffusion of all species; compare the 5/10 data in **Figure 3a** and the 10/10 data in **Figure 3c**. The

5/20 electrolyte had the slowest diffusivities, while the 10/10 electrolyte exhibited the fastest diffusivities. The spread between the specific species diffusion coefficients across all the electrolyte compositions decreases with increasing temperature. This is most clearly seen in **Figures S3-6**, where we plot the diffusivity of each ionic species as a function of temperature.

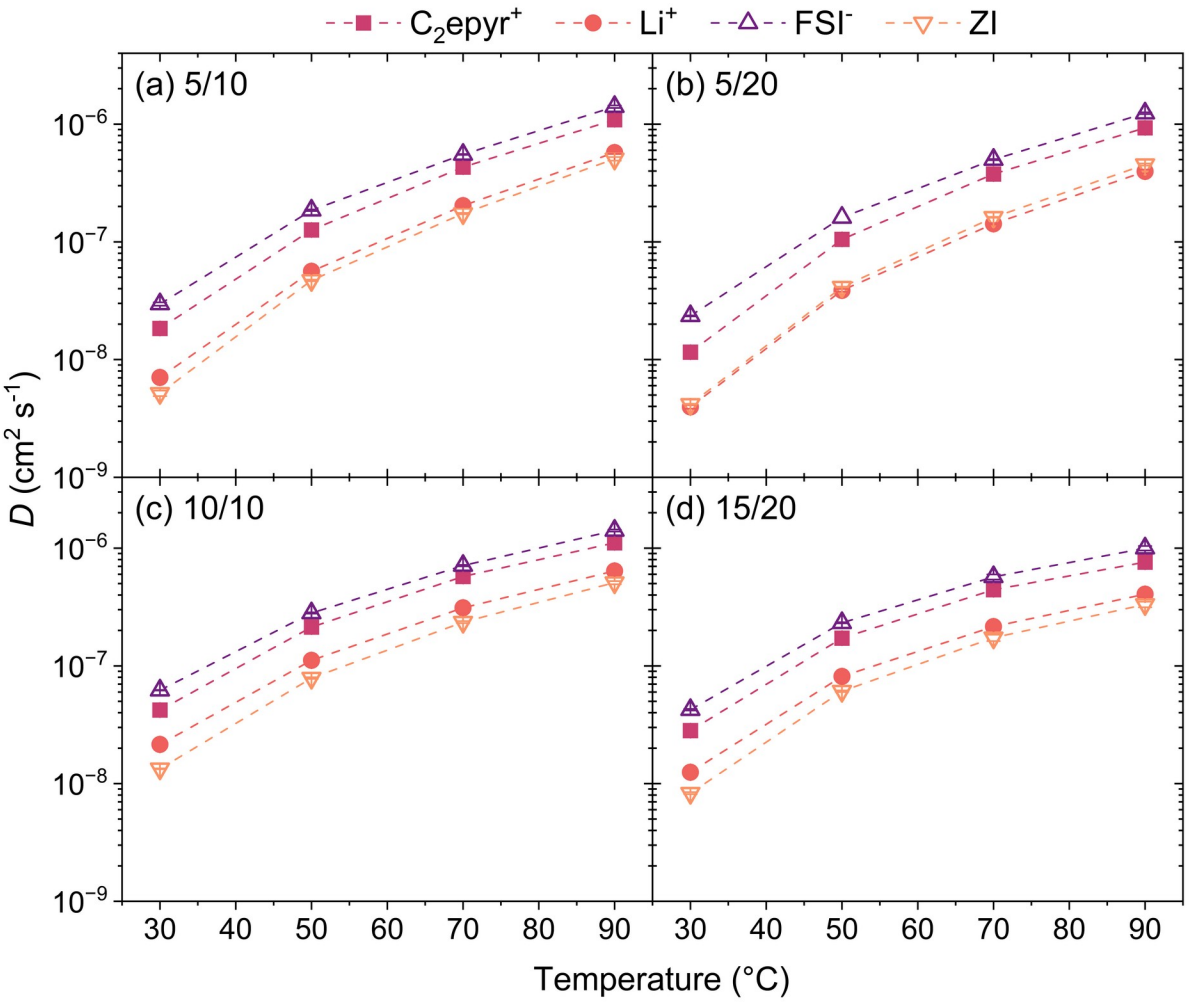

Figure 3. Self-diffusion coefficients of species in the plastic crystal electrolytes measured by pulsed-field gradient NMR versus temperature. The nuclei studied were ^{1}H, ^{7}Li, and ^{19}F. The ^{1}H and ^{7}Li spectra were used to determine $D_{C_2epyr^+}$ and D_{Li^+}. The ^{19}F spectra contained two well resolved peaks which were used to determine D_{FSI^-} and D_{ZI} (**Figure S1**). (a) 5/10 electrolyte, (b) 5/20 electrolyte, (c) 10/10 electrolyte, (d) 15/20 electrolyte. All experiments were repeated at least three times and error bars representing one standard deviation are shown. In some cases, error bars are smaller than the symbol.

Using Newman's dilute solution theory for a multicomponent electrolyte, we estimate the conductivity, σ, for an electrolyte containing three ionic species:[27]

$$\sigma = F^2 \sum_i z_i^2 u_i c_i, \qquad \textbf{(eq. 8)}$$

where z_i is the charge, u_i is the mobility, and c_i is the concentration of species i. We invoke the Nernst-Einstein relation to relate the mobility and diffusion coefficients in dilute solutions,

$$D_i = RT\, u_i. \qquad \textbf{(eq. 9)}$$

Combining **eq. 8** and **9**, we obtain:

$$\sigma = F^2 \sum_i \frac{z_i^2 D_i c_i}{RT}. \qquad \textbf{(eq. 10)}$$

When applied to the plastic crystal electrolytes, which contain three ionic species, the conductivity is described by,

$$\sigma = \frac{F^2}{RT} ¿. \qquad \textbf{(eq. 11)}$$

We also define a ratio, β, which compares the experimentally-determined ionic conductivity, κ, and estimated conductivity, σ:[58]

$$\beta = \frac{\kappa}{\sigma}. \qquad \textbf{(eq. 12)}$$

β equals one corresponds to an idealized liquid electrolyte, wherein all ionic species move independent of each other. This ratio thus provides insight into the nature of ionic correlations in plastic crystal electrolytes.

Figure 4a compares σ and κ for the 5/10 electrolyte, where we observe an order of magnitude difference in the ionic conductivities at 30°C. The comparison between σ and κ for all other electrolytes is given in **Figures S7-9**. The temperature-dependence of β of all electrolytes is given in **Figure 4b**. The electrolyte with the highest conductivity, 15/20, also exhibits the highest value of β. This suggests that the motion of ions in this electrolyte is decoupled from each other. The electrolyte with the lowest conductivity, 5/10, also exhibits the lowest value of β. One expects the value of β to increase with increasing temperature due to a decrease in the strength of ionic interactions relative to thermal energy. Contrary to this expectation, increasing the temperature of all electrolytes from 30 to 50°C results in small to no decrease in β. In the temperature range between 50 and 90°C, however, β increases with increasing temperature.

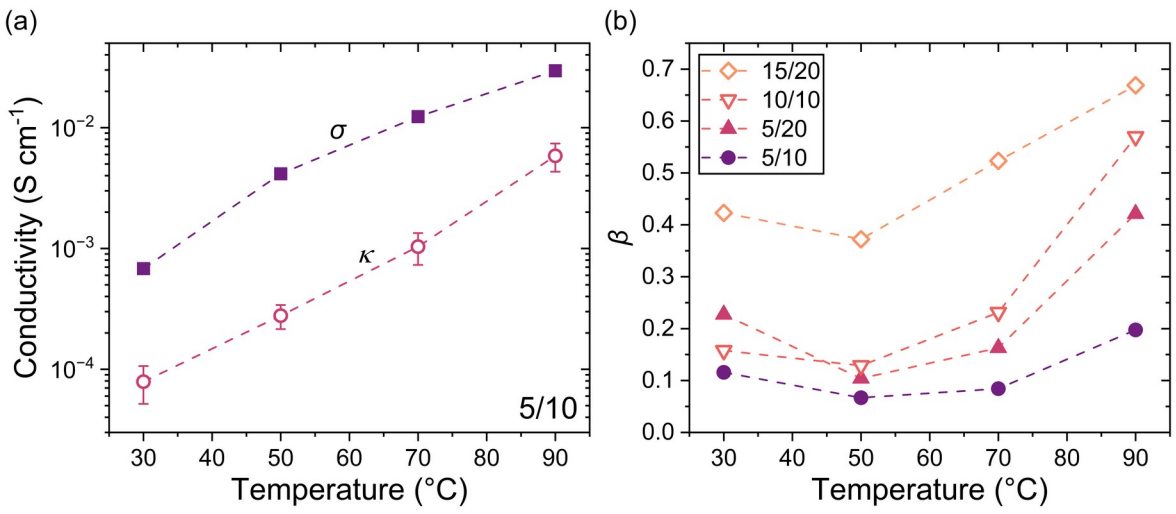

Figure 4. (a) Comparison of experimental (κ) and Newman's dilute solution theory estimate (σ) of ionic conductivity for the 5/10 electrolyte at various temperatures. (b) β ($\beta = \kappa/\sigma$) values for all plastic crystal electrolytes at various temperatures.

The current-voltage characteristics of all our electrolytes were measured using lithium symmetric cells. A constant current was applied, and the time-dependence of the cell voltage was recorded. Small changes in L are obtained across individual experiments because of slight differences in cell assembly. To account for this, and to ensure that the results obtained in this work can be readily compared to values in the literature obtained on cells with entirely different electrolyte thickness, we utilize a length-normalized form of current density, iL. Typical data obtained is shown in **Figure 5a** for selected current densities applied across the 5/10 electrolyte. The cell voltage approaches a steady plateau at low current densities of 0.23 μA cm^{-1} and below. At current densities of 1.3 μA cm^{-1} and above, we observe a divergence in the measured voltage. The time required for the cell voltage to reach 1 V is taken as the Sand's time, t_{sand}. Following the approach described in reference [29], we plot L^2/t_{sand} versus the length-normalized current density, iL for the 5/10 electrolyte in **Figure 5b**. A linear extrapolation of the data to $L^2/t_{sand} = 0$ gives the length-normalized limiting current, $i_{\lim}L$ = 1.1 ± 0.06 μA cm^{-1}. The limiting current in a given cell is inversely proportional to L.[29] The corresponding data and plots for the other plastic crystal electrolytes are given in **Figures S10-12**. The length-normalized limiting currents were estimated to be 1.1 ± 0.06 μA cm^{-1}, 1.6 ± 0.2 μA cm^{-1}, 1.6 ± 0.2 μA cm^{-1}, and 1.4 ± 0.2 μA cm^{-1} for the 5/10, 5/20, 10/10, and 15/20 electrolytes respectively.

It is instructive to compare the limiting current of plastic crystal electrolytes and that of a well-studied system, poly(ethylene oxide) bis(trifluoromethanesulfonyl)imide (PEO/LiTFSI). The limiting current of the PEO-based electrolyte at 90°C, wherein the molar ratio of lithium ions to ether oxygens is 0.1, is 30 μA cm^{-1}. The limiting current of traditional liquid electrolytes is a function of three transport parameters (κ, D, and t_{+}^{0}) and a thermodynamic factor. The parameters

that govern the limiting current in plastic crystal electrolytes have not yet been established. In the most highly conducting plastic crystal electrolyte, 15/20, $\kappa = 5.2 \times 10^{-4}$ S cm^{-1}, $\rho_+ = 0.02$, and $D = 1.5 \times 10^{-8}$ cm^2 s^{-1}. The values for PEO/LiTFSI are $\kappa = 1.5 \times 10^{-3}$ S cm^{-1}, $\rho_+ = 0.06$, and $D = 8 \times 10^{-8}$ cm^2 s^{-1}.[59] The small value of $i_{\text{lim}}L$ in all plastic crystal electrolytes relative to PEO/LiTFSI can thus be tentatively attributed to lower values of κ, ρ_+, and D. In liquid and polymer electrolyte systems, the limiting current is attributed to the formation of concentration gradients. Whether or not ionic concentration gradients are responsible for the divergence in cell voltage (e.g. **Figure 5a**) remains to be established. In principle, the concentration of both Li^+ ions and neutral zwitterions could vary across the length of the cell. These variations may induce phase transitions. There is no knowledge of the effect of dc current on the local crystal structure in plastic crystal electrolytes.

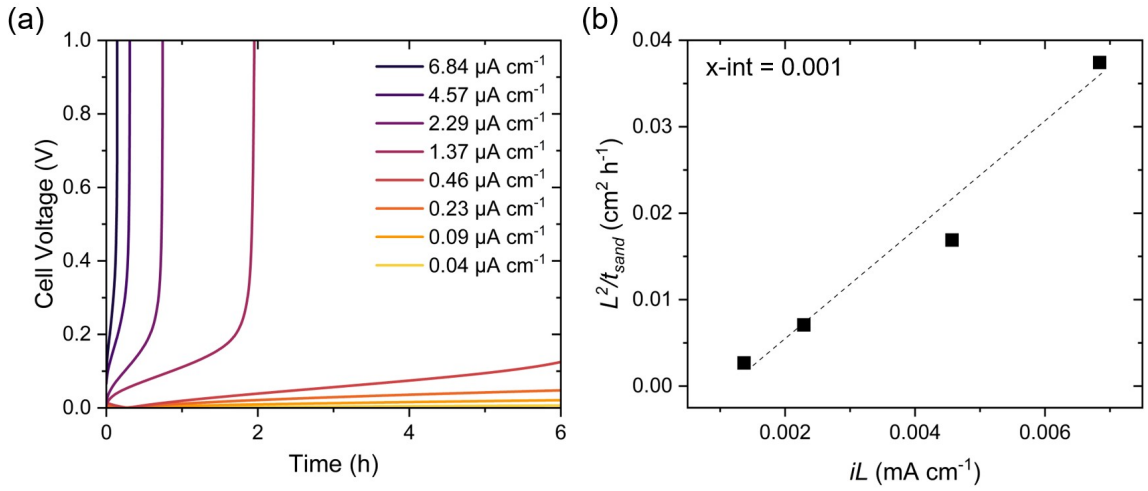

Figure 5. Experimental Sand's time measurements to estimate limiting current of the 5/10 plastic crystal electrolyte. (a) Example cell voltage (V) versus time profile for one replicate at different length-normalized current densities (iL) for the Sand's time experiments. Experiments were run for 12 h, but the time axes are limited to 6 h to highlight the divergence of V at applied currents larger than the limiting current. t_{sand} is defined as the time at which the cell voltage reaches the cutoff voltage of 1 V. (b) Plot of L^2/t_{sand} versus iL from experimental Sand's time data given in (a) used to calculate the limiting current. The x-intercept gives the length-normalized limiting current. Experiments to determine limiting current were repeated at least three times on independent cells.

We conducted *operando* WAXS to elucidate the structure of the plastic crystal electrolytes under an applied current. We focused on the 5/10 electrolyte for this study and investigated the effects of applying 11.3 μA cm^{-2} for 8 h through a lithium-indium symmetric cell, followed by 11 h at open-circuit. The applied current density corresponded to a length-normalized current density of 0.57 μA cm^{-1}, approximately 50% of the $i_{\text{lim}}L = 1.13$ μA cm^{-1} (**Figure 5**). We chose lithium-indium electrodes (instead of pure lithium) to obtain a sharp interface between the electrode and the electrolyte; the high molar mass of indium relative to lithium blocks X-ray transmission.[35] A schematic of the

operando WAXS set up is given in **Figure 6a**, and an image of the cell is provided in Figure S16. Briefly, X-rays passed through the electrolyte, parallel to the electrodes. The cell was moved in 50 µm increments along the thickness direction (x) during the electrochemical experiment, and scattering profiles were collected as a function of length-normalized spatial position (x/L) and time (t). Based on the dimensions of the cell, we collected spectra at seven positions in x/L. We present the potentiostatic data in **Figure 6b**. Initially, the cell was at open-circuit until t = 1.15 h. WAXS profiles obtained during this period were used to study the crystal structure in different locations of the cell, and evaluate how the local structure evolves with time. At t = 1.15 h, a current of 11.3 µA cm^{-2} was applied to the cell, indicated by the first dashed vertical line. The potential rose rapidly to 0.75 V due to the ohmic drop across the electrolyte and an increase in interfacial impedance (see **Figure S13**). At t = 1.7 h, the potential started to decay toward a steady-state value of 0.52 V. After 8 h of constant-current, at t = 9.15 h, the cell was allowed to relax at open-circuit as indicated by the second dashed vertical line. The cell voltage dropped rapidly to 0 V and continued to drift toward negative values. The time-dependent voltage curve from the lithium-indium symmetric WAXS cell differs from the time-dependent voltage curves obtained in lithium-symmetric cells. More work is needed to understand the origin of these differences. Nevertheless, the WAXS experiments provide structural information that cannot be gleaned from electrochemical experiments.

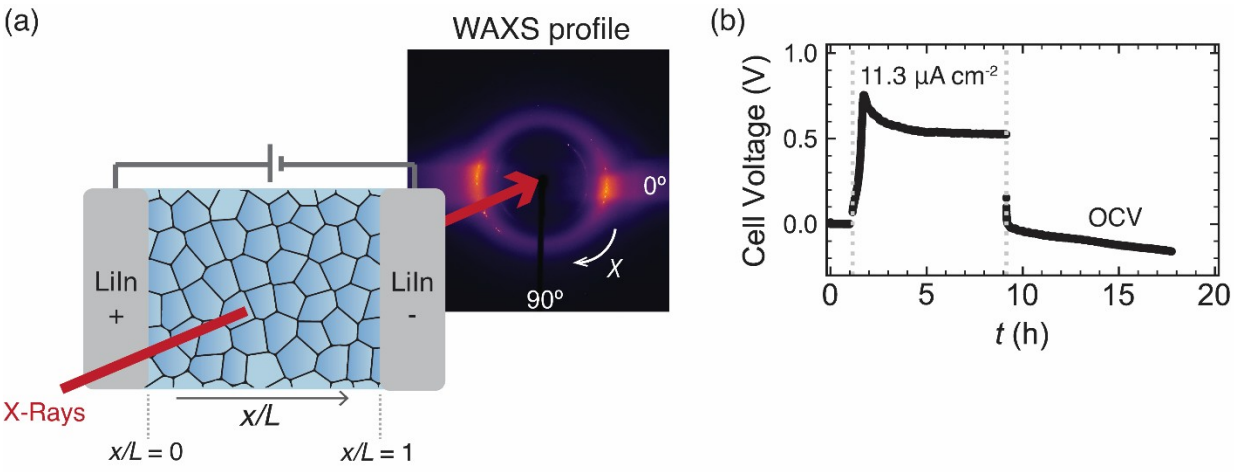

Figure 6. (a) Schematic of *operando* experiment to determine spatiotemporally-resolved WAXS profiles. The incident X-ray beam passes through the electrolyte, parallel to the electrodes, and the sample was translated in the x-direction to measure scattering profiles as a function of x/L. A sample 2D WAXS profile from the center of the cell prior to polarization is shown, along with the azimuthal coordinates. (b) Time-dependent cell voltage during the *operando* experiment. The dashed lines at t = 1.15 h and t = 9.15 h denote the start of the constant current polarizations step and the return of the cell to open-circuit. The applied current was 11.3 µA cm^{-2}, which is approximately 50% of the limiting current.

It is clear from **Figure 6a** that the scattering profiles are not azimuthally-symmetric. Any crystalline material would comprise grains oriented along different directions. If all directions were equally

represented in the scattering volume, the scattering profiles would comprise concentric rings (Debye-Scherrer rings). The presence of diffraction spots in **Figure 6a** indicates the presence of relatively large grains at specific orientations. This anisotropy is more clearly visualized in the raw spectrum and integrated plots presented in **Figure S14**. In such systems, any sample that is prepared will contain grains at different specific orientations. The measured transport properties may differ from sample to sample because transport may depend on the orientation of individual grains relative to the chosen direction of transport. In our experiments on the class of plastic crystals discussed here, most samples exhibited reproducible transport properties, which are reported above. However, we prepared several 5/0 samples (containing no zwitterion) and found conductivities that varied by an order of magnitude. We have therefore chosen not to discuss our data on this particular sample.

It is instructive to begin our discussion of the WAXS data using azimuthally-averaged intensity profiles. We turn to the WAXS results and begin by charting azimuthally-averaged intensity as a function of q over time at three representative positions in the cell: near the positive electrode, the center, and near the negative electrode (x/L = 0.2, 0.5, and 0.8, respectively). This is shown by **Figure 7**. The data in the three panels of **Figure 7** are qualitatively similar. Two dominant peaks at q = 0.85 and 1.21 $Å^{-1}$ are observed at all time points and cell positions. These scattering signatures align with the *ex situ* measurements (**Figure 1c**). The relative intensities of the two peaks, however, depend on both position and time. Before current is passed (t = 0.3 h), the high q peak is much weaker than the low q peak at x/L = 0.2 and 0.5. However, the peak intensities are comparable at x/L = 0.8. Based on this observation, we conclude that the crystals obtained at different locations in the cell are in different orientations. It is likely that this is due to the stresses applied to the electrolyte as it was loaded into the cell.

The positions of the two primary peaks do not shift significantly with the passage of current, indicating that the plastic crystal nature of the electrolyte is preserved in the presence of an applied current. However, the applied current generally leads to an increase to the intensity of the peaks; see scattering data between 2.3 and 8.5 h. In traditional liquid electrolytes, the steepest concentration gradients are obtained near the electrodes. Even near the electrodes, wherein the concentration of Li is expected to vary locally, we do not observe dramatic changes in the WAXS profiles. Returning the cell to open-circuit results in a general decrease in the intensity of the peaks. The exception is the significant increase of the low q peak between t = 12.6 and 14.6 h for x/L = 0.5.

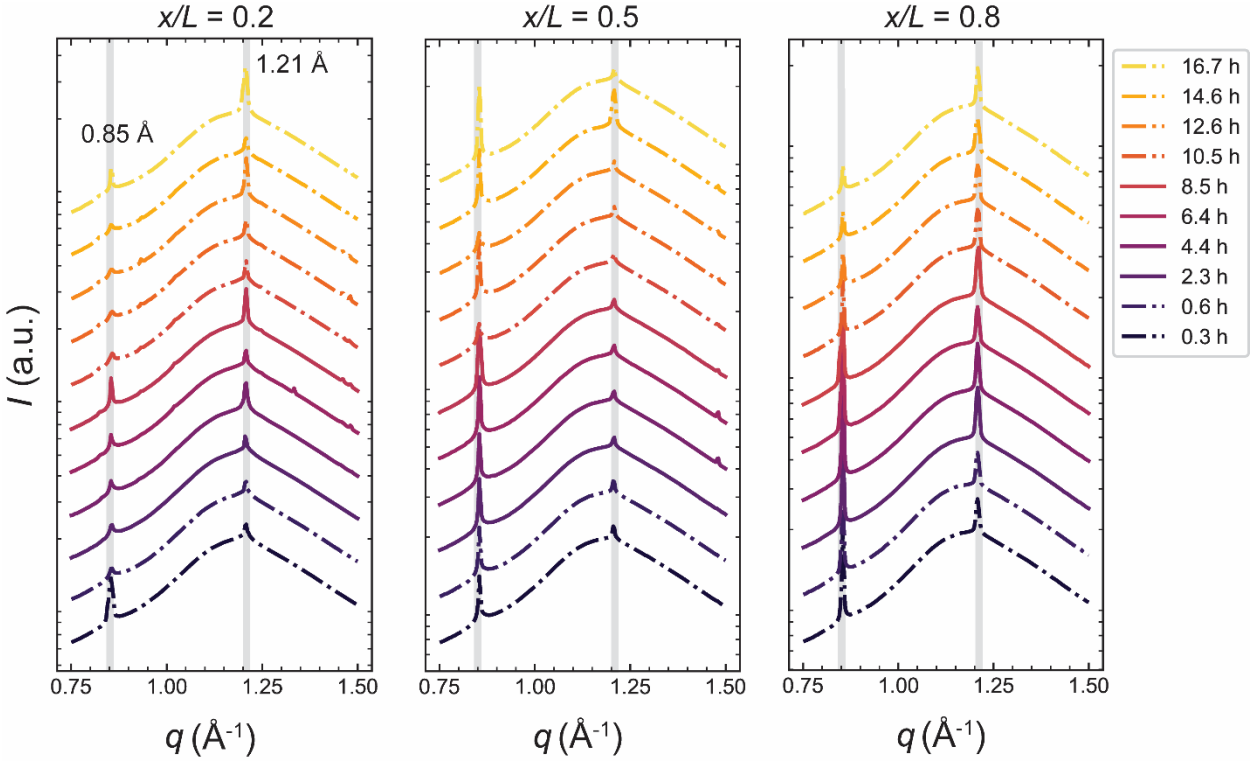

Figure 7. Azimuthally-averaged WAXS intensity as a function of q at selected times for three cell positions, x/L = 0.2, 0.5, and 0.8. Scattering profiles are shifted vertically and guiding lines at 0.85 and 1.21 Å^{-1} are added for visual clarity. Trace colors correspond to the measurement time, and electrochemical steps are designated by a solid curve for constant-current polarization and a dash-dot curve for open-circuit. The scattering from the plastic crystal electrolyte is superposed on a broad background peak due to scattering from the polycarbonate components of the *operando* cell. Example data analysis workflow is given in **Figure S14**.

To further elucidate any structural changes in the electrolyte, we tracked the intensity as a function of azimuthal angle χ at the primary q position (q = 0.85 Å^{-1}). Changes in peak intensity distributions as a function of χ generally signal rotations of crystal grains. The spatiotemporal intensity profiles as a function of χ, at the same three representative positions in the cell discussed in **Figure 7** (x/L = 0.2, 0.5, and 0.8), are given by **Figure 8**. It is evident that the electrolyte exhibits significant anisotropy prior to polarization, as shown by the bottom traces of **Figure 8** at each cell position. This is unsurprising, based on how electrolyte was loaded into the cell – in the *operando* cell, core pins exert pressure on the electrolyte faces during assembly. However, the dependence of intensity on χ changes with time, even before the current is turned on. This can be noted with the disappearance of a peak at 330° between t = 0.3 and 0.6 h at x/L = 0.2. This indicates that the stresses used to load the sample do not dissipate quickly. We posit that the plastic crystal grains at a given location in the cell undergo rotations due to these residual stresses.

After current is turned on, several peaks appear and disappear at specific values of χ, signaling continued rotation of the plastic crystal grains. However, there is a general increase in peak intensities as current is passed. Returning the cell to open circuit results in an overall decrease in scattering intensity with some exceptions (e.g. the 14.6 and 16.7 h data at x/L = 0.2 and 0.5).

A clearer view of the effect of ionic current on crystal structure is obtained by examining a limited range of χ values. In **Figure 9a**, we show the data between χ = 170 and 210° at x/L = 0.2. The applied current increases the peak intensity at χ = 176° from t = 2.3 to 6.4 h. However, the peak intensity decreases between 6.4 and 8.5 h. The applied current also produces small additional peaks between 193 and 206°. The current-induced peaks in this range of χ persist after the cell is returned to open-circuit. In **Figure 9b**, we show the data between χ = 20 and 50° at x/L = 0.8. Here, we see that applying current leads to an increase in the intensity of the peaks at χ = 36 and 46°. These current-induced peaks diminish significantly in intensity after the cell is returned to open-circuit.

It is not trivial to obtain an overall picture of current-induced morphological changes in the 5/10 plastic crystal electrolyte. The complexity of the data in **Figures 6-9** is bewildering. Lacking a better alternative, we examined the spatiotemporal dependence of the intensity-weighted average of χ, $\overline{\chi}$:

$$\overline{\chi}(x,t)=\frac{\sum_{0°}^{360°}\chi I(\chi;x,t)}{\sum_{0°}^{360°} I(\chi;x,t)}. \qquad \textbf{(eq. 13)}$$

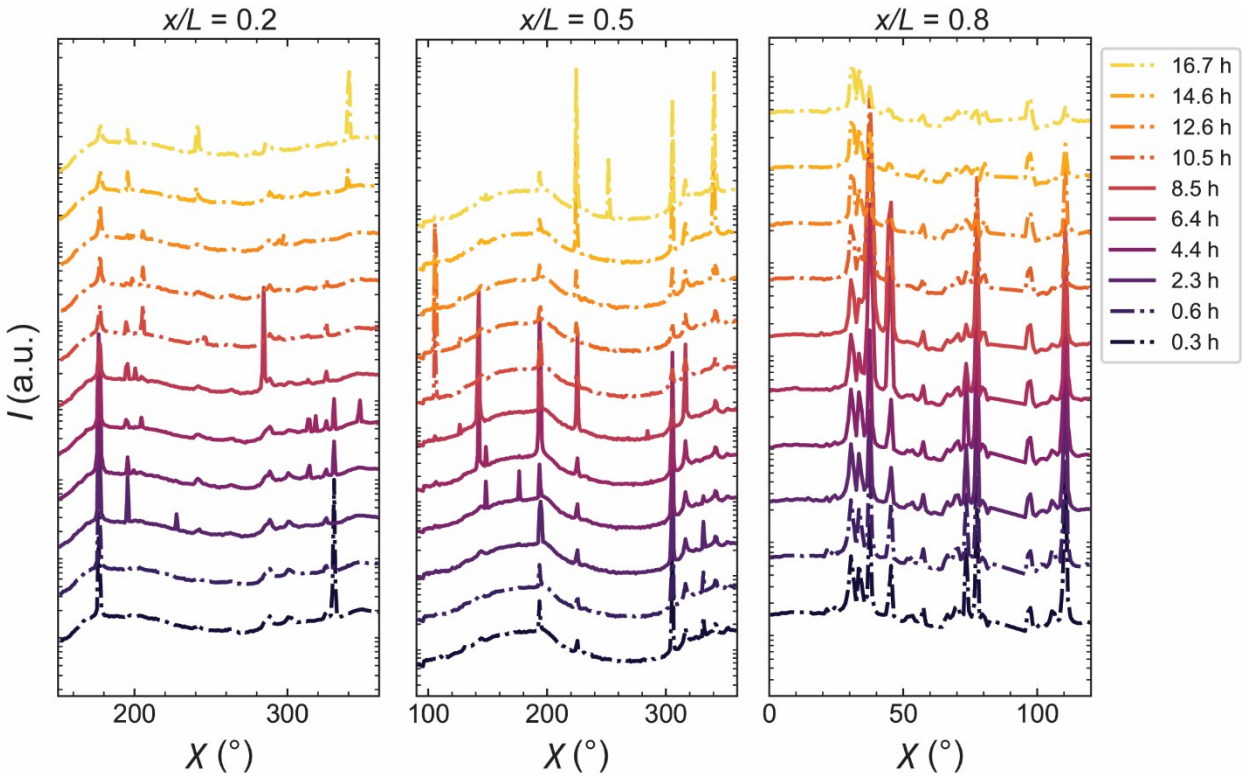

Figure 8. WAXS intensity I for the peak at $q = 0.85$ Å^{-1} as a function of azimuthal angle χ at selected times for three cell positions, x/L = 0.2, 0.5, and 0.8. Scattering spectra are shifted vertically for visual clarity. Trace colors correspond to the measurement time, and electrochemical steps are designated by a solid curve for constant-current polarization and a dash-dot curve for open-circuit. The x-axis limits were chosen to highlight regions where clear changes in the WAXS profiles were evident. The full spectra from $\chi = 0°$ to 360° at all locations are given in **Figure S15**.

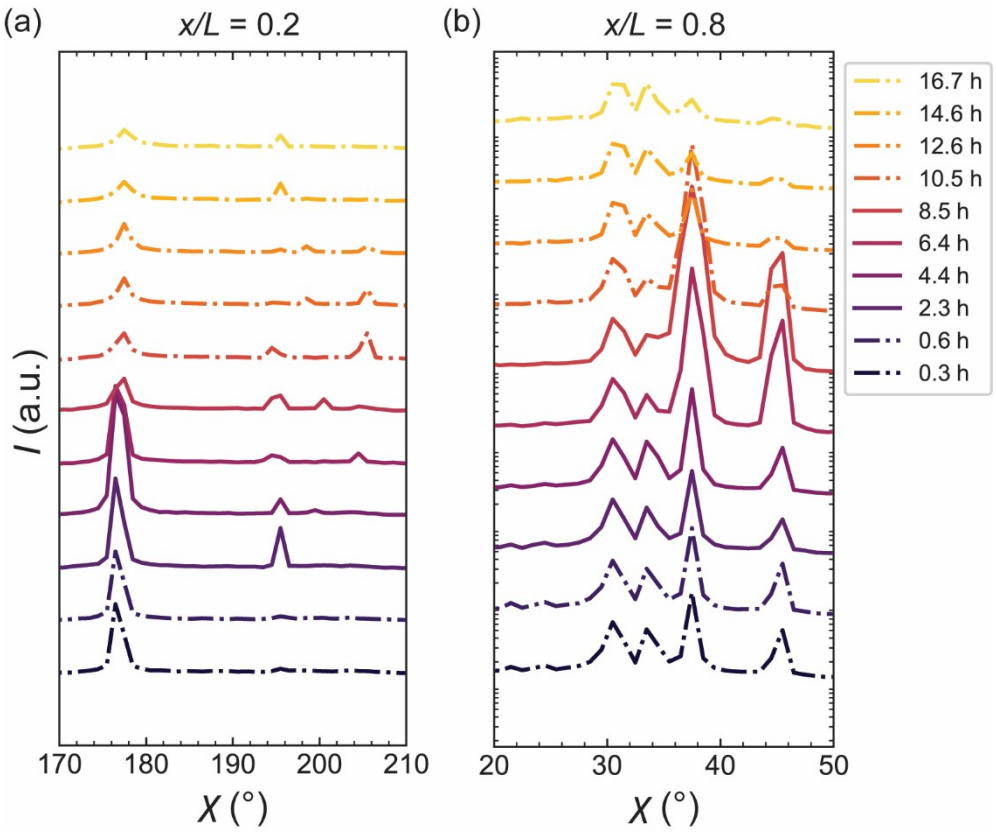

Figure 9. WAXS intensity I for the peak at $q = 0.85$ Å^{-1} as a function of azimuthal angle χ at selected times for x/L = (a) 0.2 and (b) 0.8. The x-axis limits are subsets of **Figure 8** to clarify changes in peak intensity. Scattering spectra are shifted vertically for visual clarity. Trace colors correspond to the measurement time, and electrochemical steps are designated by a solid curve for constant-current polarization and a dash-dot curve for open-circuit.

In **Figures 8-9**, we examine the variables that affect the intensity at $q = 0.85$ Å^{-1} as a function of azimuthal angle, location, and time. In **eq. 13**, we defined the intensity-weighted average of $\overline{\chi}$ for these results. A simple measure of the overall rotation of crystal grains is obtained by computing $\Delta\overline{\chi}$, defined as

$$\Delta\overline{\chi}(x,t) = \overline{\chi}(x,t) - \overline{\chi}(x,0) \qquad \textbf{(eq. 14)}$$

The time-dependence of $\Delta\overline{\chi}$ obtained at different values of x/L is plotted in **Figure 10**, alongside the time-dependence of the cell potential. The dashed vertical lines denote the start of the constant-current polarization and return to open-circuit. The evolution of local structure was tracked using $\Delta\overline{\chi}$. When current was applied, $\Delta\overline{\chi}$ near the positive electrode ($0.2 \leq x/L \leq 0.5$) was negligible (**Figure 10b**). Near the negative electrode ($0.6 \leq x/L \leq 0.8$), however, $\Delta\overline{\chi}$ remained at zero for the first five hours of polarization but drifted significantly in the last four hours of polarization, attaining a value of -70° at the end of polarization (**Figure 10c**). When the cell was returned to open-circuit, the $\Delta\overline{\chi}$ values near the negative electrode returned to zero. Surprisingly, near the

positive electrode, $\Delta\overline{\chi}$, which was zero for about five hours after the return to open-circuit, drifted towards +70° during the last three hours at open-circuit. Qualitatively speaking, the WAXS results provide insight into the effect of applied current on the crystal structure of plastic crystal electrolytes. Perhaps the main difference between liquid electrolytes and plastic crystal electrolytes is that, in the case of liquid electrolytes, the applied current causes translation of the ions towards the positive electrode, while in the plastic crystal electrolytes, the applied current causes rotation in the crystal grains. The mechanisms which underlie these rotations are complex, and we posit that they arise from the formation of local stresses in these systems. These stresses provide an additional pathway for energy dissipation and efficiency loss through the electrolyte.

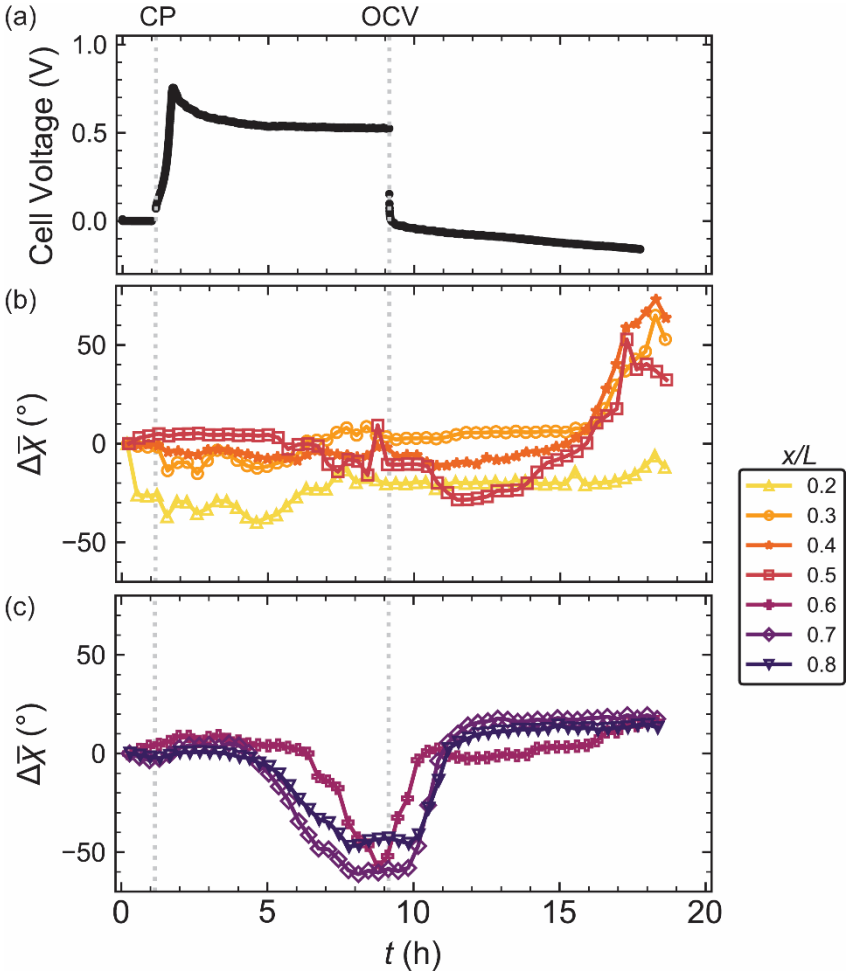

Figure 10. (a) Time-dependence of cell potential over *operando* experiment. Time-dependence of $\Delta\overline{\chi}$ for the 5/10 electrolyte at q = 0.85 Å^{-1} for (b) 0.2 ≤ x/L ≤ 0.5 and (c) 0.6 ≤ x/L ≤ 0.8. The constant-current (CP) and open-circuit (OCV) steps are marked by the dashed vertical lines.

Conclusions

A series of electrolytes were obtained by adding a lithium salt and a zwitterion to a pyrrolidinium-based organic ionic plastic crystal. While conductivity could be improved by increasing salt and zwitterion concentrations, all electrolytes exhibited unexpectedly low current fraction values on the order of 0.02. In alignment with these low current fraction values, the electrolytes also displayed low limiting currents, as estimated via Sand's time measurements. Our electrochemical results highlight that ionic conductivity alone is a poor metric for electrolyte performance. We conclude that none of the plastic crystal electrolytes studied here would support practically relevant current densities in rechargeable batteries.

Using PFG-NMR, we measured the self-diffusion coefficients of the cationic C_2epyr^+ and Li^+, the anionic FSI^-, and the zwitterion species. We observed that the addition of zwitterion decreased the diffusivity of the Li^+ relative to the other ionic species. Thus, the improved ionic conductivity in the presence of zwitterion may compromise Li^+ transference. A rigorous understanding of Li^+ transference in plastic crystal electrolytes requires quantification of field-induced velocities of all species, which we have not yet measured. While the PFG-NMR experiments confirm that all species are mobile under quiescent conditions, the relative mobility of the species under applied electric fields has not yet been established. The PFG-NMR results are, at best, indirectly related to cation transference.

We turned to *operando* WAXS to probe spatiotemporal structure of the plastic crystal electrolyte under an applied field. The structure was probed at a current density that was 50% of the limiting current. It is apparent that the response of plastic crystals to an applied current can be complex and irreversible. During polarization, significant rotation of the plastic crystal grains occurs near the negative electrode. After returning the cell to open-circuit, the plastic crystals in this region spring back to their quiescent state. In contrast, during polarization, negligible changes in plastic crystal structure are observed near the positive electrode. After returning the cell to open-circuit, the plastic crystals in this region rotate to an angle that is equal and opposite to that found in the negative electrode region at the end of polarization. It is likely that these complex observations are related to current-induced local stresses in these systems.

In simple electrolytes comprising three mobile species, Newman's concentrated solution theory enables prediction of ion transport with the knowledge of three transport properties, ionic conductivity, diffusion coefficient, and cation transference number, and two thermodynamic properties, the salt activity coefficient and the partial molar volume of the salt. Ion transport in plastic crystal electrolytes is governed by these transport and thermodynamic parameters, as well as the characteristics of the crystalline phase. It is often difficult to compare the efficacy of ion transport across different plastic crystals because improvements in one parameter, such as conductivity, often come at the expense of another. $i_{\mathrm{lim}}L$ = 1.6 μA cm^{-1} will serve as a simple benchmark for evaluating the efficacy of next-generation plastic crystal electrolytes and will allow for comparison across different classes of solid electrolytes. Extending concentrated solution

theory to include the presence of crystals is necessary for a deeper understanding of the mechanistic underpinnings of ion motion in plastic crystal electrolytes.

Supplementary Information

Sample PFG-NMR spectra, fittings, and full self-diffusion coefficient results; full comparisons of experimental ionic conductivity and Nernstian conductivities across all electrolyte compositions; Sand's time estimations of limiting current across all electrolyte compositions, Nyquist plot for custom *operando* cell impedance; sample workup of *operando* WAXS spectra and full spectra of intensity versus azimuthal angle over three cell positions; measurements of electrolyte density

Acknowledgements

The authors gratefully acknowledge financial support from the Mitsubishi Chemical Center for Advanced Materials (MC-CAM). EEA was supported by the National Science Foundation Graduate Research Fellowship Program under Grant No. DGE 2146752. Any opinions, findings, and conclusions or recommendations expressed in this material are those of the author(s) and do not necessarily reflect the views of the National Science Foundation. DSC experiments at the Molecular Foundry were supported by the Office of Science, Office of Basic Energy Sciences, of the U.S. Department of Energy under Contract No. DE-AC02-05CH11231, under proposal number MFP-10100. *Ex situ* and *operando* WAXS measurements were done at SSRL beamline 11-3. Use of the Stanford Synchrotron Radiation Lightsource, SLAC National Accelerator Laboratory, is supported by the U.S. Department of Energy, Office of Science, Office of Basic Energy Sciences under Contract No. DE-AC02-76SF00515. We thank Dr. Raynald Giovine, and Pines Magnetic Resonance Center's Core NMR Facility (PMRC Core) for spectroscopic assistance. The NMR instrument used in this work is supported by the National Science Foundation under Grant No. 2018784. The authors acknowledge Prof. Shrayesh Patel (University of Chicago) for insightful conversations.

1 List of Symbols

c	Concentration (mol L^{-1})
[C_2epyr][FSI]	*N,N*-diethylpyrrolidinium bis(fluorosulfonyl)imide
C_I	Centroid of scattering intensity over χ (°)
D	Diffusion coefficient (cm^2 s^{-1})
D_i	Self-diffusion coefficient of species i from PFG-NMR (cm^2 s^{-1})
d	Interplane spacing (Å)
dc	Direct current
DSC	Differential scanning calorimetry
F	Faraday's constant (96,485 C mol^{-1})
I	Scattering intensity (a.u.), function of q and/or χ
i	Current density (mA cm^{-2})
L	Thickness of electrolyte (electrode-to-electrode distance) (cm)
LiFSI	Lithium bis(fluorosulfonyl)imide salt
M_{Li}	Molar mass of LiFSI salt (187.07 g mol^{-1})
M_{IPC}	Molar mass of [C_2epyr][FSI] plastic crystal (308.36 g mol^{-1})
M_{ZI}	Molar mass of zwitterion additive (324.36 g mol^{-1})
PFG-NMR	Pulse-field gradient nuclear magnetic resonance spectroscopy
PyFAI	Python fast azimuthal integrator WAXS analysis package
q	Scattering vector ($Å^{-1}$)
r	Molar ratio of lithium to ether oxygens in the electrolyte ([Li^+]/[EO])
r_i	Molar ratio of species i (e.g. LiFSI, ZI) to [C_2epyr][FSI] in the electrolyte
t	Time (h)
WAXS	Wide-angle X-ray scattering
x	Position in the electrolyte along the direction of ion transport

x/L	Position in the electrolyte normalized by the electrolyte thickness
ZI	Zwitterion additive ((3-(1-methylpyrrolidin-1-ium-1-yl)propyl)sulfonyl) ((trifluoromethyl)sulfonyl)imide

1 Greek Letters

β	Ratio of experimental and theoretical conductivities
κ	Ionic conductivity (S cm^{-1})
π	Mathematical constant (3.14159)
ρ	Electrolyte density (kg L^{-1})
σ	Nernst-Einstein estimated conductivity (S cm^{-1})
χ	Azimuthal angle of 2D scattering (°)
$\overline{\chi}$	Intensity-weighted average of χ (°)
$\Delta\overline{\chi}$	Time-dependent change of $\overline{\chi}$ (°)

2

3

References

(1) Liu, Y.-K.; Zhao, C.-Z.; Du, J.; Zhang, X.-Q.; Chen, A.-B.; Zhang, Q. Research Progresses of Liquid Electrolytes in Lithium-Ion Batteries. *Small* **2023**, *19* (8), 2205315. https://doi.org/10.1002/smll.202205315.

(2) Chen, X.; Guan, Z.; Chu, F.; Xue, Z.; Wu, F.; Yu, Y. Air-Stable Inorganic Solid-State Electrolytes for High Energy Density Lithium Batteries: Challenges, Strategies, and Prospects. *InfoMat* **2022**, *4* (1), e12248. https://doi.org/10.1002/inf2.12248.

(3) Wang, X.; Kerr, R.; Chen, F.; Goujon, N.; Pringle, J. M.; Mecerreyes, D.; Forsyth, M.; Howlett, P. C. Toward High-Energy-Density Lithium Metal Batteries: Opportunities and Challenges for Solid Organic Electrolytes. *Adv. Mater.* **2020**, *32* (18), 1905219. https://doi.org/10.1002/adma.201905219.

(4) Dai, T.; Wu, S.; Lu, Y.; Yang, Y.; Liu, Y.; Chang, C.; Rong, X.; Xiao, R.; Zhao, J.; Liu, Y.; Wang, W.; Chen, L.; Hu, Y.-S. Inorganic Glass Electrolytes with Polymer-like Viscoelasticity. *Nat. Energy* **2023**, *8* (11), 1221–1228. https://doi.org/10.1038/s41560-023-01356-y.

(5) Kato, Y.; Hori, S.; Saito, T.; Suzuki, K.; Hirayama, M.; Mitsui, A.; Yonemura, M.; Iba, H.; Kanno, R. High-Power All-Solid-State Batteries Using Sulfide Superionic Conductors. *Nat. Energy* **2016**, *1* (4), 16030. https://doi.org/10.1038/nenergy.2016.30.

(6) Patel, V.; Lee, O.; Makkar, S.; Balsara, N. P. Ion Transport in Concentrated Crosslinked Solid Polymer Electrolytes. *J. Electrochem. Soc.* **2025**, *172* (12), 120517. https://doi.org/10.1149/1945-7111/ae285f.

(7) Shpigel, N.; Levi, M. D.; Sigalov, S.; Daikhin, L.; Aurbach, D. In Situ Real-Time Mechanical and Morphological Characterization of Electrodes for Electrochemical Energy Storage and Conversion by Electrochemical Quartz Crystal Microbalance with Dissipation Monitoring. *Acc. Chem. Res.* **2018**, *51* (1), 69–79. https://doi.org/10.1021/acs.accounts.7b00477.

(8) Bucci, G.; Swamy, T.; Bishop, S.; Sheldon, B. W.; Chiang, Y.-M.; Carter, W. C. The Effect of Stress on Battery-Electrode Capacity. *J. Electrochem. Soc.* **2017**, *164* (4), A645. https://doi.org/10.1149/2.0371704jes.

(9) Zhao, Q.; Pan, L.; Li, Y.; Chen, L.; Shi, S. Rotational Motion of Polyanion versus Volume Effect Associated with Ionic Conductivity of Several Solid Electrolytes. *Rare Met.* **2018**, *37* (6), 497–503. https://doi.org/10.1007/s12598-018-1058-2.

(10) Dixit, M. B.; Singh, N.; Horwath, J. P.; Shevchenko, P. D.; Jones, M.; Stach, E. A.; Arthur, T. S.; Hatzell, K. B. In Situ Investigation of Chemomechanical Effects in Thiophosphate Solid Electrolytes. *Matter* **2020**, *3* (6), 2138–2159. https://doi.org/10.1016/j.matt.2020.09.018.

(11) Pringle, J. M.; Howlett, P. C.; MacFarlane, D. R.; Forsyth, M. Organic Ionic Plastic Crystals: Recent Advances. *J. Mater. Chem.* **2010**, *20* (11), 2056. https://doi.org/10.1039/b920406g.

(12) L. Thomas, M.; Hatakeyama-Sato, K.; Nanbu, S.; Yoshizawa-Fujita, M. Organic Ionic Plastic Crystals: Flexible Solid Electrolytes for Lithium Secondary Batteries. *Energy Adv.* **2023**, *2* (6), 748–764. https://doi.org/10.1039/D3YA00078H.

(13) Jin, L.; C. Howlett, P.; M. Pringle, J.; Janikowski, J.; Armand, M.; R. MacFarlane, D.; Forsyth, M. An Organic Ionic Plastic Crystal Electrolyte for Rate Capability and Stability of Ambient Temperature Lithium Batteries. *Energy Environ. Sci.* **2014**, *7* (10), 3352–3361. https://doi.org/10.1039/C4EE01085J.

(14) Basile, A.; Hilder, M.; Makhlooghiazad, F.; Pozo-Gonzalo, C.; MacFarlane, D. R.; Howlett, P. C.; Forsyth, M. Ionic Liquids and Organic Ionic Plastic Crystals: Advanced Electrolytes for Safer High Performance Sodium Energy Storage Technologies. *Adv. Energy Mater.* **2018**, *8* (17), 1703491. https://doi.org/10.1002/aenm.201703491.
(15) Dahbi, M.; Ghamouss, F.; Tran-Van, F.; Lemordant, D.; Anouti, M. Comparative Study of EC/DMC LiTFSI and LiPF6 Electrolytes for Electrochemical Storage. *J. Power Sources* **2011**, *196* (22), 9743–9750. https://doi.org/10.1016/j.jpowsour.2011.07.071.
(16) Makhlooghiazad, F.; C. Howlett, P.; Wang, X.; Hilder, M.; R. MacFarlane, D.; Armand, M.; Forsyth, M. Phosphonium Plastic Crystal Salt Alloyed with a Sodium Salt as a Solid-State Electrolyte for Sodium Devices: Phase Behaviour and Electrochemical Performance. *J. Mater. Chem. A* **2017**, *5* (12), 5770–5780. https://doi.org/10.1039/C6TA10340E.
(17) Seeber, A. J.; Forsyth, M.; Forsyth, C. M.; Forsyth, S. A.; Annat, G.; MacFarlane, D. R. Conductivity, NMR and Crystallographic Study of N,N,N,N-Tetramethylammonium Dicyanamide Plastic Crystal Phases: An Archetypal Ambient Temperature Plastic Electrolyte Material. *Phys. Chem. Chem. Phys.* **2003**, *5* (12), 2692–2698. https://doi.org/10.1039/B212743A.
(18) Yunis, R.; Al-Masri, D.; Hollenkamp, A. F.; Doherty, C. M.; Zhu, H.; Pringle, J. M. Plastic Crystals Utilising Small Ammonium Cations and Sulfonylimide Anions as Electrolytes for Lithium Batteries. *J. Electrochem. Soc.* **2020**, *167* (7), 070529. https://doi.org/10.1149/1945-7111/ab76a2.
(19) Zhu, H.; Huang, G.; O'Dell, L. A.; Forsyth, M. New Insights into Decoupled Cation and Anion Transport and Dynamic Heterogeneity in a Diethyl(Methyl)(Isobutyl)Phosphonium Hexafluorophosphate Organic Ionic Plastic Crystal. *J. Phys. Chem. Lett.* **2021**, *12* (40), 9853–9858. https://doi.org/10.1021/acs.jpclett.1c02943.
(20) Armel, V.; Velayutham, D.; Sun, J.; C. Howlett, P.; Forsyth, M.; R. MacFarlane, D.; M. Pringle, J. Ionic Liquids and Organic Ionic Plastic Crystals Utilizing Small Phosphonium Cations. *J. Mater. Chem.* **2011**, *21* (21), 7640–7650. https://doi.org/10.1039/C1JM10417A.
(21) Jin, L.; Nairn, K. M.; Forsyth, C. M.; Seeber, A. J.; MacFarlane, D. R.; Howlett, P. C.; Forsyth, M.; Pringle, J. M. Structure and Transport Properties of a Plastic Crystal Ion Conductor: Diethyl(Methyl)(Isobutyl)Phosphonium Hexafluorophosphate. *J. Am. Chem. Soc.* **2012**, *134* (23), 9688–9697. https://doi.org/10.1021/ja301175v.
(22) Armel, V.; Velayutham, D.; Sun, J.; Howlett, P. C.; Forsyth, M.; MacFarlane, D. R.; Pringle, J. M. Ionic Liquids and Organic Ionic Plastic Crystals Utilizing Small Phosphonium Cations. *J. Mater. Chem.* **2011**, *21* (21), 7640–7650. https://doi.org/10.1039/C1JM10417A.
(23) Zhou, Y.; Wang, X.; Zhu, H.; Armand, M.; Forsyth, M.; Greene, G. W.; Pringle, J. M.; Howlett, P. C. N-Ethyl-N-Methylpyrrolidinium Bis(Fluorosulfonyl)Imide-Electrospun Polyvinylidene Fluoride Composite Electrolytes: Characterization and Lithium Cell Studies. *Phys. Chem. Chem. Phys.* **2017**, *19* (3), 2225–2234. https://doi.org/10.1039/C6CP07415D.
(24) Yamada, H.; Miyachi, Y.; Takeoka, Y.; Rikukawa, M.; Yoshizawa-Fujita, M. Pyrrolidinium-Based Organic Ionic Plastic Crystals: Relationship between Side Chain Length and Properties. *Electrochimica Acta* **2019**, *303*, 293–298. https://doi.org/10.1016/j.electacta.2019.02.076.
(25) Bachman, J. C.; Muy, S.; Grimaud, A.; Chang, H.-H.; Pour, N.; Lux, S. F.; Paschos, O.; Maglia, F.; Lupart, S.; Lamp, P.; Giordano, L.; Shao-Horn, Y. Inorganic Solid-State

Electrolytes for Lithium Batteries: Mechanisms and Properties Governing Ion Conduction. *Chem. Rev.* **2016**, *116* (1), 140–162. https://doi.org/10.1021/acs.chemrev.5b00563.
(26) Balsara, N. P.; Newman, J. Divergence of Velocity Fields in Electrochemical Systems. *J. Electrochem. Soc.* **2022**, *169* (7), 070535. https://doi.org/10.1149/1945-7111/ac8246.
(27) Newman, J.; Balsara, N. P. *Electrochemical Systems*, Fourth edition.; The electrochemical society series; Wiley: Hoboken, NJ, 2021.
(28) Abdo, E. E.; Patel, V.; Mistry, A.; Takacs, C. J.; Balsara, N. P. Mapping Spatiotemporal Solvent Velocity from Measured Concentration Gradients in a Polarized Electrolyte. *J. Electrochem. Soc.* **2025**, *172* (2), 020510. https://doi.org/10.1149/1945-7111/adacb0.
(29) Hoffman, Z. J.; Mistry, A.; Srinivasan, V.; Balsara, N. P. Comparing Experimentally-Measured Sand's Times with Concentrated Solution Theory Predictions in a Polymer Electrolyte. *J. Electrochem. Soc.* **2023**, *170* (12), 120524. https://doi.org/10.1149/1945-7111/ad1470.
(30) Phiri, I.; Bon, C. Y.; Mwemezi, M.; Hamenu, L.; Madzvamuse, A.; Park, J. H.; Lee, K. S.; Ko, J. M.; Lu, Y. Enhanced Electrolyte Performance by Adopting Zwitterionic Lithium-Silica Sulfobetaine Silane as Electrolyte Additive for Lithium-Ion Batteries. *Mater. Chem. Phys.* **2020**, *243*, 122577. https://doi.org/10.1016/j.matchemphys.2019.122577.
(31) Ohno, H.; Yoshizawa, M.; Ogihara, W. A New Type of Polymer Gel Electrolyte: Zwitterionic Liquid/Polar Polymer Mixture. *Electrochimica Acta* **2003**, *48* (14), 2079–2083. https://doi.org/10.1016/S0013-4686(03)00188-9.
(32) Sun, J.; Bayley, P.; MacFarlane, D. R.; Forsyth, M. Gel Electrolytes Based on Lithium Modified Silica Nano-Particles. *Electrochimica Acta* **2007**, *52* (24), 7083–7090. https://doi.org/10.1016/j.electacta.2007.05.033.
(33) Makhlooghiazad, F.; O'Dell, L. A.; Porcarelli, L.; Forsyth, C.; Quazi, N.; Asadi, M.; Hutt, O.; Mecerreyes, D.; Forsyth, M.; Pringle, J. M. Zwitterionic Materials with Disorder and Plasticity and Their Application as Non-Volatile Solid or Liquid Electrolytes. *Nat. Mater.* **2022**, *21* (2), 228–236. https://doi.org/10.1038/s41563-021-01130-z.
(34) Ilavsky, J. It Nika: Software for Two-Dimensional Data Reduction. *J. Appl. Crystallogr.* **2012**, *45* (2), 324–328. https://doi.org/10.1107/S0021889812004037.
(35) Abdo, E. E.; Patel, V.; Hesse, S. A.; Dudchenko, A. V.; Arthur, R. J.; Takacs, C. J.; Balsara, N. P. Tracking Spatiotemporal Electric Potential in Batteries Using High-Resolution Operando X-Ray Transmission Imaging. *J. Phys. Chem. C* **2025**, *129* (45), 20112–20122. https://doi.org/10.1021/acs.jpcc.5c05969.
(36) Kieffer, J.; Karkoulis, D. PyFAI, a Versatile Library for Azimuthal Regrouping. *J. Phys. Conf. Ser.* **2013**, *425* (20), 202012. https://doi.org/10.1088/1742-6596/425/20/202012.
(37) Bruce, P. G.; Vincent, C. A. Steady State Current Flow in Solid Binary Electrolyte Cells. *J. Electroanal. Chem. Interfacial Electrochem.* **1987**, *225* (1), 1–17. https://doi.org/10.1016/0022-0728(87)80001-3.
(38) Newman, J.; Chapman, T. W. Restricted Diffusion in Binary Solutions. *AIChE J.* **1973**, *19* (2), 343–348. https://doi.org/10.1002/aic.690190220.
(39) Pagès, G.; Gilard, V.; Martino, R.; Malet-Martino, M. Pulsed-Field Gradient Nuclear Magnetic Resonance Measurements (PFG NMR) for Diffusion Ordered Spectroscopy (DOSY) Mapping. *Analyst* **2017**, *142* (20), 3771–3796. https://doi.org/10.1039/C7AN01031A.

(40) Han, K. S.; Bazak, J. D.; Chen, Y.; Graham, T. R.; Washton, N. M.; Hu, J. Z.; Murugesan, V.; Mueller, K. T. Pulsed Field Gradient Nuclear Magnetic Resonance and Diffusion Analysis in Battery Research. *Chem. Mater.* **2021**, *33* (22), 8562–8590. https://doi.org/10.1021/acs.chemmater.1c02891.
(41) Sinnaeve, D. The Stejskal–Tanner Equation Generalized for Any Gradient Shape—an Overview of Most Pulse Sequences Measuring Free Diffusion. *Concepts Magn. Reson. Part A* **2012**, *40A* (2), 39–65. https://doi.org/10.1002/cmr.a.21223.
(42) Forsyth, M.; Chimdi, T.; Seeber, A.; Gunzelmann, D.; Howlett, P. C. Structure and Dynamics in an Organic Ionic Plastic Crystal, N-Ethyl-N-Methyl Pyrrolidinium Bis(Trifluoromethanesulfonyl) Amide, Mixed with a Sodium Salt. *J. Mater. Chem. A* **2014**, *2* (11), 3993–4003. https://doi.org/10.1039/C3TA15153K.
(43) Abeysooriya, S.; Makhlooghiazad, F.; Chotard, J.-N.; O'Dell, L. A.; Pringle, J. M. Investigation of the Physicochemical Properties of Pyrrolidinium-Based Mixed Plastic Crystal Electrolytes. *J. Phys. Chem. C* **2023**, *127* (25), 12304–12320. https://doi.org/10.1021/acs.jpcc.3c02249.
(44) Boynton, N.; Hess, L.; Dutta, S.; Kuwana, C.; Mirmira, P.; Solymosy, G.; Filatov, A.; Hagan, T.; Bartridge, S.; Rambo, A.; Dibeh, J.; Vivod, S.; Abdulahad, A.; Amanchukwu, C.; Ferguson, A.; Rowan, S.; Patel, S. Influence of Thermal Processing and Doping Concentration on Phase Behaviour of a Lithium-Transporting Organic Ionic Plastic Crystal. *ChemRxiv*. July 29, 2025. https://doi.org/10.26434/chemrxiv-2025-b2jmw. (accessed 2025-09-24).
(45) Phiri, I.; Bon, C. Y.; Kim, S.; Mwemezi, M.; Hamenu, L.; Madzvamuse, A.; Kim, S. H.; Ko, J. M. Effects of Novel Benzotriazole Based Zwitterionic Salt as Electrolyte Additive for Lithium Ion Batteries. *Curr. Appl. Phys.* **2020**, *20* (1), 122–131. https://doi.org/10.1016/j.cap.2019.10.017.
(46) Suematsu, M.; Yoshizawa-Fujita, M.; Tamura, T.; Takeoka, Y.; Rikukawa, M. Dependence of Transport Properties of Concentrated Lithium Salt Solutions on Temperature and Composition in an Imidazolium-Based Liquid Zwitterion Containing an Oligo(Ethylene Oxide) Unit. *Int. J. Electrochem. Sci.* **2015**, *10* (1), 248–258. https://doi.org/10.1016/S1452-3981(23)04990-8.
(47) Huang, J.; Hill, A.; Forsyth, M.; MacFarlane, D.; Hollenkamp, A. Conduction in Ionic Organic Plastic Crystals: The Role of Defects. *Solid State Ion.* **2006**, *177* (26), 2569–2573. https://doi.org/10.1016/j.ssi.2006.01.041.
(48) Zhu, H.; MacFarlane, D. R.; Pringle, J. M.; Forsyth, M. Organic Ionic Plastic Crystals as Solid-State Electrolytes. *Trends Chem.* **2019**, *1* (1), 126–140. https://doi.org/10.1016/j.trechm.2019.01.002.
(49) Jin, L.; Howlett, P.; Efthimiadis, J.; Kar, M.; Macfarlane, D.; Forsyth, M. Lithium Doped N,N-Dimethyl Pyrrolidinium Tetrafluoroborate Organic Ionic Plastic Crystal Electrolytes for Solid State Lithium Batteries. *J. Mater. Chem.* **2011**, *21* (27), 10171. https://doi.org/10.1039/c0jm04401f.
(50) Doyle, M.; Fuller, T. F.; Newman, J. The Importance of the Lithium Ion Transference Number in Lithium/Polymer Cells. *Electrochimica Acta* **1994**, *39* (13), 2073–2081. https://doi.org/10.1016/0013-4686(94)85091-7.

(51) Diederichsen, K. M.; Fong, K. D.; Terrell, R. C.; Persson, K. A.; McCloskey, B. D. Investigation of Solvent Type and Salt Addition in High Transference Number Nonaqueous Polyelectrolyte Solutions for Lithium Ion Batteries. *Macromolecules* **2018**, *51* (21), 8761–8771. https://doi.org/10.1021/acs.macromol.8b01696.
(52) Kato, Y.; Watanabe, M.; Sanui, K.; Ogata, N. Ionic Transport Number of Network PEO Electrolytes. *Solid State Ion.* **1990**, *40–41*, 632–636. https://doi.org/10.1016/0167-2738(90)90085-6.
(53) Buss, H. G.; Chan, S. Y.; Lynd, N. A.; McCloskey, B. D. Nonaqueous Polyelectrolyte Solutions as Liquid Electrolytes with High Lithium Ion Transference Number and Conductivity. *ACS Energy Lett.* **2017**, *2* (2), 481–487. https://doi.org/10.1021/acsenergylett.6b00724.
(54) Hirotsu, Y.; Kimura, M.; Nanbu, S.; Takeoka, Y.; Rikukawa, M.; Yoshizawa-Fujita, M. Enhanced Ion-Transport Characteristics of Pyrrolidinium-Based Electrolytes with Mg(FSA)2. *Phys. Chem. Chem. Phys.* **2025**, *27* (26), 13826–13835. https://doi.org/10.1039/D5CP01386K.
(55) Wohde, F.; Balabajew, M.; Roling, B. Li+ Transference Numbers in Liquid Electrolytes Obtained by Very-Low-Frequency Impedance Spectroscopy at Variable Electrode Distances. *J. Electrochem. Soc.* **2016**, *163* (5), A714. https://doi.org/10.1149/2.0811605jes.
(56) Brinkkötter, M.; Mariani, A.; Jeong, S.; Passerini, S.; Schönhoff, M. Ionic Liquid in Li Salt Electrolyte: Modifying the Li+ Transport Mechanism by Coordination to an Asymmetric Anion. *Adv. Energy Sustain. Res.* **2021**, *2* (2), 2000078. https://doi.org/10.1002/aesr.202000078.
(57) Nordness, O.; Gordon, L. W.; Zhang, Z.; Ganesan, V.; Clément, R. J. Disentangling Cation Effects on Ion Mobility and Structure in Ionic Liquid Electrolytes. *J. Phys. Energy* **2026**, *8* (1), 015019. https://doi.org/10.1088/2515-7655/ae3c3f.
(58) Timachova, K.; Chintapalli, M.; Olson, K. R.; Mecham, S. J.; DeSimone, J. M.; Balsara, N. P. Mechanism of Ion Transport in Perfluoropolyether Electrolytes with a Lithium Salt. *Soft Matter* **2017**, *13* (32), 5389–5396. https://doi.org/10.1039/C7SM00794A.
(59) Gao, K. W.; Balsara, N. P. Electrochemical Properties of Poly(Ethylene Oxide) Electrolytes above the Entanglement Threshold. *Solid State Ion.* **2021**, *364*, 115609. https://doi.org/10.1016/j.ssi.2021.115609.

1 **ToC graphic**

2